Ab Initio Self-Trapped Excitons

Yunfei Bai,[1,2] Yaxian Wang,[1,*] and Sheng Meng[1,2,3,†]
[1]*Beijing National Laboratory for Condensed Matter Physics and Institute of Physics, Chinese Academy of Sciences, Beijing 100190, China*
[2]*School of Physical Sciences, University of Chinese Academy of Sciences, Beijing 100190, China*
[3]*Songshan Lake Materials Laboratory, Dongguan, Guangdong 523808, China*

(Received 3 December 2023; accepted 14 June 2024; published 26 July 2024)

We propose a new formalism and an effective computational framework to study self-trapped excitons (STEs) in insulators and semiconductors from first principles. Using the many-body Bethe-Salpeter equation in combination with perturbation theory, we are able to obtain the mode- and momentum-resolved exciton-phonon coupling matrix element in a perturbative scheme and explicitly solve the real space localization of the electron (hole), as well as the lattice distortion. Further, this method allows us to compute the STE potential energy surface and evaluate the STE formation energy and Stokes shift. We demonstrate our approach using two-dimensional magnetic semiconductor chromium trihalides and a wide-gap insulator BeO, the latter of which features dark excitons, and make predictions of their Stokes shift and coherent phonon generation which we hope will spark future experiments such as photoluminescence and transient absorption studies.

DOI: 10.1103/PhysRevLett.133.046903

Excitons, a quasiparticle composed of correlated electron-hole pairs, embrace rich many-body physics and play a crucial role in semiconductor science and technology. As a fundamental quasiparticle, excitons can interact with the lattice degree of freedom, or phonons. Exciton-phonon interaction gives rise to a wide range of emergent phenomena such as phonon-induced exciton linewidth [1], phonon side bands [2], phonon replica [3], valley polarized exciton relaxation [4], etc. Apart from these effects, strong exciton-phonon interaction can lead to a self-trapped exciton (STE), i.e., an exciton trapped on its own lattice distortion field [5–8], which can dramatically influence luminescence, energy transport, and formation of lattice defects in crystals. The STE is usually signaled by photoluminescence with a large and broadened Stokes shift, and coherent phonon generation which can be observed through transient absorption spectroscopy. STEs have been observed in various materials, including alkali halides and oxides [9–12], two-dimensional (2D) chromium trihalides which have gained great research interest recently [13–18], the promising photovoltaic material $CsPbBr_3$ [19], and hybrid organic perovskites [20]. Manipulating STE formation and their properties can further inspire new device concepts. Their broad emission band, high photoluminescence quantum efficiency, and large tunability show promises for optical device applications such as light-emitting diodes [21,22], luminescent solar concentrators [23], and efficient photovoltaic cells [24].

Microscopically, the formation of STEs can be understood from the Franck-Condon principle, as schematically illustrated in Fig. 1. Though well observed experimentally, an *ab initio* description of STEs that properly accounts for the electron-hole correlation and exciton-phonon interaction with full lattice degree of freedom is still lacking and remains a daunting task, with some major challenges as follows. First, although the supercell technique for

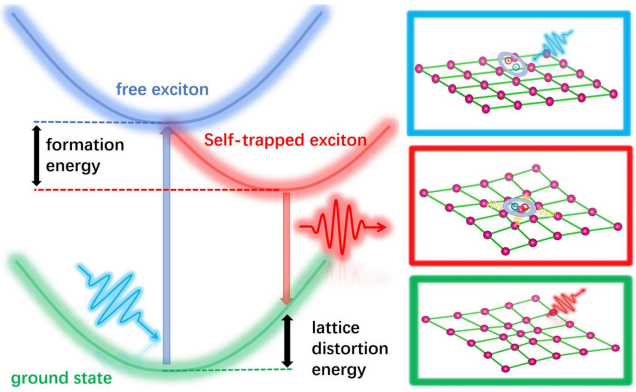

FIG. 1. Schematics showing the Franck-Condon picture of the STE formation. The green, blue, and red curves in the left-hand panel correspond to the PES of the ground state, the free exciton state, and the STE state, respectively. The right-hand panel illustrates interactions involved during the formation and decay of STE. Top: a semiconducting or insulating material is optically excited, generating a free exciton. Middle: the exciton is trapped by a localized lattice distortion, forming an STE state. Bottom: the STE decays with a lower-energy photon emitted, causing a Stokes shift as part of its energy is released to the lattice.

*Contact author: yaxianw@iphy.ac.cn
†Contact author: smeng@iphy.ac.cn

calculating polarons, i.e., a quasiparticle formed by an excess electron (hole) with lattice distortion, has been widely applied [25,26], the computational cost of the *GW* with Bethe-Salpeter equation (BSE) approach makes the STE calculation using supercells impractical. Second, previous studies mainly adopt constrained density functional theory for lattice relaxation, then use BSE with the distorted lattice to calculate the exciton binding energy and photoluminescence spectrum [27]. The major drawback here is that missing the excitonic effect in the first place may lead to unrealistic lattice distortion, especially for strongly correlated Frenkel excitons.

Herein, we propose an *ab initio* framework that properly treats both the excitonic effect and its coupling to all phonon modes, based on the many-body *GW*-BSE method [28–30] in combination with density functional perturbation theory [31]. After benchmarking the STE lattice configuration in Li_2O_2, we present calculations for 2D magnetic chromium trihalides, using $CrBr_3$ as a prototypical example. We then study monolayer BeO, a system featuring dark exciton state. For both systems, we explicitly calculate the mode- and momentum-resolved exciton-phonon coupling strength in the momentum space, from which we obtain the real-space electron (hole) localization and the STE potential energy surfaces. Our method overcomes the difficulties concerning atomic force calculations in the presence of excitons and properly takes the many-body effects into account at a reasonable computational cost. It also allows us to explore a large configuration phase space, which is important to achieve realistic results. Finally, our approach can be easily applied to other semiconductors and insulators.

Theoretical framework—We start from a perturbation-theory-based framework, which has been applied to compute polaron formation [10,11], where the total energy of a polaronic system can be described as a summation of its ground state energy and a linear expansion with respect to the lattice displacement:

$$E\{\tau,\psi\} = E\{\tau^0,\psi^0\} + \frac{1}{2}C_{\kappa_1\alpha i,\kappa_2\beta j}\tau_{\kappa_1\alpha i}\tau_{\kappa_2\beta j} + \int \psi^*\left[H^0_{\mathrm{KS}} + \frac{\partial V^0_{\mathrm{KS}}}{\partial\tau_{\kappa_1\alpha i}}\tau_{\kappa_1\alpha i}\right]\psi. \quad (1)$$

Here ψ is the excess electron's wave function, $\tau_{\kappa\alpha i}$ the atomic displacement with $\kappa\alpha i$ denoting the Cartesian coordinate α of atom κ in the ith unit cell. H^0_{KS}, $(\partial V^0_{\mathrm{KS}}/\partial\tau_{\kappa_1\alpha i})$, and $\psi^0_{n\mathbf{k}}$ are the ground state Kohn-Sham (KS) Hamiltonian, the variation of the KS potential, and the wave function with band index n and wave vector $\mathbf{k}$, respectively. $C_{\kappa_1\alpha i,\kappa_2\beta j}$ represents the force constant matrix. Einstein summation convention is assumed throughout the text unless otherwise specified.

The total energy for an exciton-phonon coupled system can be expressed by replacing the KS Hamiltonian with the many-body BSE Hamiltonian and the electronic wave function by its exciton counterpart,

$$E\{\tau,\psi_{\mathrm{ex}}\} = E\{\tau^0,\psi^0_{\mathrm{ex}}\} + \frac{1}{2}C_{\kappa_1\alpha i,\kappa_2\beta j}\tau_{\kappa_1\alpha i}\tau_{\kappa_2\beta j} + \int \psi^*_{\mathrm{ex}}\left[H_{\mathrm{BSE}} + \frac{\partial H_{\mathrm{BSE}}}{\partial\tau_{\kappa_1\alpha i}}\tau_{\kappa_1\alpha i}\right]\psi_{\mathrm{ex}}, \quad (2)$$

where ψ^0_{ex} denotes the exciton empty state. The BSE Hamiltonian can be written as $H^{\mathrm{BSE}}_{vc,v'c'} = (\varepsilon_c - \varepsilon_v)\delta_{cc'}\delta_{vv'} + (2V_{vc,v'c'} - W_{vc,v'c'})$, with W and V representing the direct electron-electron attraction and the exchange term, respectively. c (c') and v (v') are the conduction and valence band indices.

Applying the principles of energy minimization and exciton number conservation to Eq. (2), we reach the following self-consistent eigenequations:

$$\frac{2}{N_p}B_{\mathbf{q}\mu}G^{\text{ex-ph}}_{nm\mu}(\mathbf{Q},\mathbf{q})A_{m\mathbf{Q}+\mathbf{q}} = (\varepsilon_{n\mathbf{Q}} - \varepsilon)A_{n\mathbf{Q}},$$
$$B_{\mathbf{q}\mu} = \frac{1}{N_p}A^*_{m\mathbf{Q}+\mathbf{q}}\frac{G^{\text{ex-ph}}_{nm\mu}(\mathbf{Q},\mathbf{q})}{\hbar\omega_{\mathbf{q}\mu}}A_{n\mathbf{Q}}. \quad (3)$$

Here N_p is the number of unit cells in the supercell. $A_{n\mathbf{Q}}$ denotes the STE wave function in the exciton basis, with $B_{\mathbf{q}\mu}$ the lattice wave function in the phonon eigenmode basis. The exciton-phonon coupling matrix $G^{\text{ex-ph}}_{nm\mu}(\mathbf{Q},\mathbf{q})$ is by definition the differential of the BSE Hamiltonian with respect to the lattice displacement along a phonon normal mode. Assuming constant static screening function, one can estimate the $G^{\text{ex-ph}}_{nm\mu}(\mathbf{Q},\mathbf{q})$ using the exciton wave function in the electron-hole pair basis $E^{n\mathbf{Q}}_{v\mathbf{k},c\mathbf{k}+\mathbf{Q}}$ and electron-phonon coupling matrix $g^{\text{el-ph}}$ by [32,33]

$$G^{\text{ex-ph}}_{nm\mu}(\mathbf{Q},\mathbf{q}) = E^{m\mathbf{Q}+\mathbf{q}*}_{v\mathbf{k},c\mathbf{k}+\mathbf{Q}+\mathbf{q}}E^{n\mathbf{Q}}_{v\mathbf{k},c'\mathbf{k}+\mathbf{Q}}g^{\text{el-ph}}_{c'c\mu}(\mathbf{k}+\mathbf{Q},\mathbf{q}) - E^{m\mathbf{Q}+\mathbf{q}*}_{v\mathbf{k}-\mathbf{q},c\mathbf{k}+\mathbf{Q}}E^{n\mathbf{Q}}_{v'\mathbf{k},c\mathbf{k}+\mathbf{Q}}g^{\text{el-ph}}_{vv'\mu}(\mathbf{k}-\mathbf{q},\mathbf{q}), \quad (4)$$

where m and n denote the exciton band indices and $\mathbf{Q}$ is the exciton center-of-mass momentum.

We note that the above equations are obtained under the approximation that both phonons and the electron-phonon coupling lie in the linear regime, in other words, under small lattice distortion. Further, this requires well-defined exciton states, i.e., strong enough Coulomb interaction to maintain the exciton quasiparticle. We therefore can first solve the BSE equation to obtain the lowest exciton bands, and then treat the exciton-phonon interaction perturbatively.

Solving Eq. (3) gives the STE (phonon) wave function $A_{n\mathbf{Q}}$ ($B_{\mathbf{q}\mu}$) and allows us to calculate the real-space lattice distortion associated with the STE formation by

$$\tau_{\kappa\alpha i} = -\frac{2}{N_p}B^*_{\mathbf{q}\mu}\left(\frac{\hbar}{2M_\kappa\omega_{\mathbf{q}\mu}}\right)^{1/2}\mathbf{e}_{\kappa\alpha\mu}(\mathbf{q})e^{i\mathbf{q}\cdot\mathbf{R}_i}, \quad (5)$$

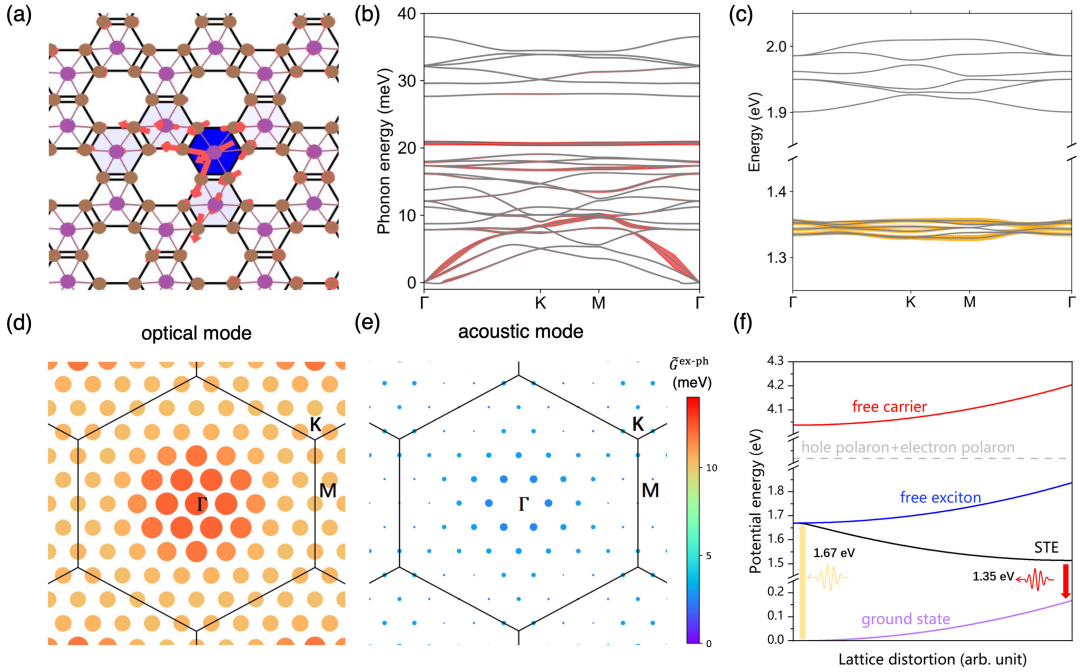

FIG. 2. STE in monolayer $CrBr_3$. (a) The calculated atomic displacements on an 8×8 supercell of monolayer $CrBr_3$, labeled by red arrows. Purple (brown) circles represent the Cr (Br) atoms, respectively. The blue color map shows the hole density distribution, highlighting its real-space localization. (b) Phonon dispersion of monolayer $CrBr_3$ with its linewidth proportional to the amplitude of $|B_{\mathbf{q}\mu}|^2$. (c) Exciton bands of monolayer $CrBr_3$, with the radii of the circles proportional to the amplitude of $|A_{n\mathbf{Q}}|^2$. (d),(e) Distribution of the exciton-phonon coupling strength in the Brillouin zone for the flat optical and acoustic LA phonon modes, respectively. The color of markers indicates the value of $\tilde{G}^{\text{ex-ph}}(\mathbf{q})$ while the size represents the phonon-frequency-normalized value $(|\tilde{G}^{\text{ex-ph}}_{\mu}(\mathbf{q})|^2/\omega_{\mathbf{q}\mu})$. (f) PES for various states. The STE state (black curve) significantly lowers the total energy in comparison to the free exciton state (blue curve). Optical transition for the STE shows a redshift of 0.32 eV in comparison with the free exciton, shown by the bold arrows to guide the eye.

with M_κ being the ion mass, $\mathbf{R}_i$ the direct lattice vector, $\mathbf{e}_{\kappa\alpha\mu}$ the phonon normal mode with branch μ, wave vector $\mathbf{q}$, and frequency $\omega_{\mathbf{q}\mu}$.

As such, our method offers another advantage to explore the PES of the free exciton and STE states by non-self-consistently solving the first eigenequation in Eq. (3) with a certain lattice distortion. Otherwise, it can only be obtained from the finite displacement method using a large supercell, which suffers from a limited phonon phase space.

Furthermore, the "localization" of the STE state can be seen more clearly from the electron and hole distribution. To this end, we obtain the STE wave function by further expanding the electron and hole Bloch wave functions following $|\Psi_{\text{STE}}\rangle = \lambda^{ck_2}_{vk_1}|ck_2\rangle\langle vk_1|$, with the coefficient $\lambda^{ck_2}_{vk_1} = A_{n\mathbf{Q}}E^{n\mathbf{Q}}_{vk_1,ck_2}$ $(\mathbf{Q} = k_2 - k_1)$. Since the electron and hole states are entangled, we take advantage of the Wannier representation and calculate the reduced density matrix of the electron (hole) by tracing out the hole (electron) to reflect their real-space wave functions, i.e., $\hat{\rho}_{\text{hole}} = \lambda^{ck}_{v_1k_1}\lambda^{ck*}_{v_2k_2}|v_2k_2\rangle\langle v_1k_1|$ and $\hat{\rho}_{\text{electron}} = \lambda^{c_1k_1}_{vk}\lambda^{c_2k_2*}_{vk}|c_1k_1\rangle\langle c_2k_2|$. Finally, we arrive at

$$\rho^{jw_2}_{iw_1} = \langle jw_2|\hat{\rho}_{\text{hole or electron}}|iw_1\rangle. \tag{6}$$

Here, i (j) denotes the unit cell index and w denotes the Wannier function index. The diagonal part of the reduced density matrix is the classical contribution to the electron (hole) density, and the off-diagonal part is the quantum coherence which leads to local density fluctuations.

The simulation flowchart of our framework is provided in the Supplemental Material (SM) Sec. S1 [34], along with the scripts [48]. As a benchmark, we achieve tractable results in Li_2O_2. Specifically, we obtain highly localized lattice distortion manifesting in a large O–O bond length change of 0.49 Å [0.48 Å obtained by delta self-consistent field calculations [12]]. Moreover, we uncover from the mode-resolved coupling strength that the two high frequency optical phonons dominate the STE wave function, which implies a Holstein-like interaction. By comparing the STE formation energy with that of the separated electron polaron and hole polaron, it can be inferred that the STE in Li_2O_2 can be considered as an electron polaron tightly bound with a hole through the electron-hole Coulomb interaction (for more details, see SM Sec. S3 [34]).

STE in monolayer $CrBr_3$—Bulk $CrBr_3$ crystallizes in the trigonal $R\bar{3}m$ space group, and its monolayer contains edge-sharing $CrBr_6$ octahedra where Cr is bonded to six equivalent Br atoms. G_0W_0 calculation yields a band gap of 4.04 eV for monolayer $CrBr_3$, while BSE on top of G_0W_0

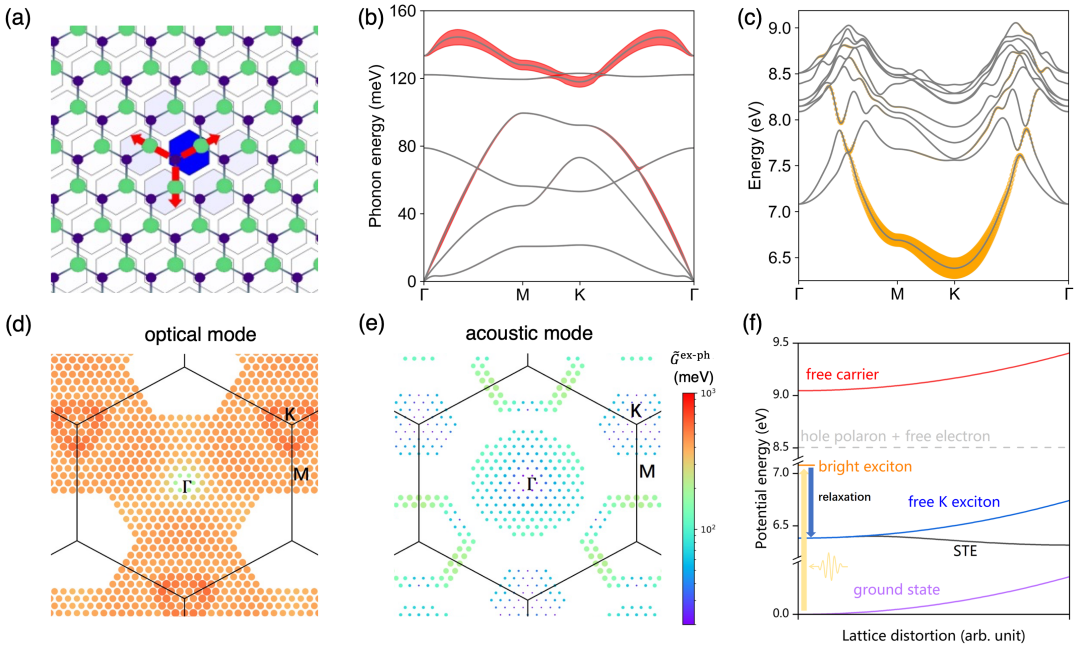

FIG. 3. STE in monolayer BeO. (a) The calculated atomic displacements on a 24×24 supercell of monolayer BeO, labeled by red arrows. Green (dark blue) circles represent the Be (O) atoms. The blue color map shows the hole density distribution, highlighting its real-space localization. (b) Phonon dispersion of monolayer BeO with its linewidth proportional to the amplitude of $|B_{\mathbf{q}\mu}|^2$. (c) Exciton bands of monolayer BeO, with the radii of the circles proportional to the amplitude of $|A_{n\mathbf{Q}}|^2$. Note the exciton bands in BeO are highly dispersed with the global minimum located at K. (d),(e) Distribution of the exciton-phonon coupling strength in the Brillouin zone for the optical and acoustic phonon modes, respectively. Color coding and marker size follow the definition of that in Figs. 2(d) and 2(e). (f) PES for various states. The STE state (black curve) lowers the total energy in comparison to both the free exciton (blue curve) and the hole polaron with an excess electron (gray dashed line). The bold arrows highlight the optical transition of the bright exciton at 7.08 eV before relaxing to the dark exciton through coupling to phonons.

gives the lowest exciton peak at 1.35 eV (for computational details, see SM Sec. S2 [34]). Our calculation gives an STE formation energy of 156 meV in $CrBr_3$. In combination with the lattice distortion energy of 168 meV, a Stokes shift of 324 meV is expected, in excellent agreement with the experimental observation of 320 meV [49]. Figure 2(f) explicitly shows the PESs for the free carrier, the free exciton, and the STE states with respect to lattice distortion, with the electron (hole) polaron state marked by a dashed line for reference. One can see that the STE state is much more energetically favorable than the polaron state. Another feature that can be observed is that the PES of the STE state has a significantly slower change at the energy minimum than the lattice distortion energy, meaning a small variation in STE energy can lead to a large variation of Stokes shift. This naturally explains the large full width at half maximum (FWHM) observed in the photoluminescence spectra [49].

Figures 2(b) and 2(c) show the phonon and exciton dispersion, on top of which we overlay the STE wave function in the exciton and phonon basis, to present the mode- and momentum-resolved contribution to the STE formation. One can see that the exciton bands in $CrBr_3$ are remarkably flat, with a dispersion width of less than 10 meV [Fig. 2(c)]. Such flat exciton bands are a result of the flat valance and conduction bands in $CrBr_3$ (SM Fig. S4 [34]), which could in turn facilitate the STE formation by expanding the exciton-phonon phase space. As for the lattice, apart from the low-energy longitudinal acoustic (LA) mode making a noticeable contribution to the STE formation, two almost degenerate flat phonon bands at ~20.58 meV also have a strong coupling strength, corresponding to the in-plane and out-of-plane breathing motion of the Cr-Br octahedra. It has been observed that similar phonon modes are excited coherently when the STE is formed in CrI_3 [27]. The real-space lattice distortion is shown by the red arrows in Fig. 2(a), each of which denotes our calculated atomic displacement by Eq. (5). The distortion is rather localized at the bound electron-hole pair, for which we show the hole distribution in blue shading.

We further plot the distribution of the averaged exciton-phonon coupling strength $\tilde{G}^{\text{ex-ph}}$ for the phonon modes strongly coupled to the exciton state of interest at $\mathbf{Q_0}$ in the entire Brillouin zone, which we define as $(1/N_b)\sqrt{\Sigma_{nm}|G^{\text{ex-ph}}_{nm\mu}(\mathbf{Q_0},\mathbf{q})|^2}$. Here N_b is the number of the lowest exciton bands among which the average is taken. As can be seen in Figs. 2(d) and 2(e), the flat optical mode

exhibits larger and more uniform distribution coupling strength. Together with the well localized exciton and lattice distortion, as well as the short-range nature of exciton-phonon interaction, we believe our method successfully captures the STE formation in monolayer $CrBr_3$ (for detailed results of $CrCl_3$, see SM Sec. S4 [34]).

STE in monolayer BeO—Recently, monolayer BeO was synthesized through the epitaxial growth method [50], which broadens the 2D materials phase space beyond being limited to their existing bulk layered counterparts. BeO has a honeycomb lattice similar to that of hexagonal boron nitride (*h*-BN). As an insulator, it has a wide band gap (> 5 eV), suggesting it is likely to exhibit a significant excitonic effect. Moreover, a recent work reports a localized hole polaron with formation energy of over 500 meV in 2D BeO, indicating strong electron-phonon coupling [51]. These facts motivate us to study the STE formation and make predictions that we hope can be verified by future experiments.

Density functional theory level calculation shows a direct gap of 5.85 eV and an indirect gap of 5.36 eV in monolayer BeO. G_0W_0 calculation yields an overall band gap correction of around 3.7 eV (for computational details, see SM Sec. S2 [34]). BSE calculation results in the lowest bright exciton at 7.08 eV with a binding energy of 2.5 eV. Such a large binding energy implies that the lowest-energy exciton in monolayer BeO is most likely Frenkel type, though a Wannier-Mott-type exciton cannot be ruled out in lower-dimensional materials. Using the same approach, we obtain an STE formation energy of 66 meV, with a lattice distortion energy of 360 meV. Further, we find the STE is ∼2 eV more stable than a hole polaron with a free electron. Thus, the STE is unlikely to be broken down by strong interaction with the lattice; therefore, monolayer BeO may serve as an ideal test bed for STE formation.

From the phonon dispersion in Fig. 3(b), we see that both LA and LO (longitudinal optical) phonons play a major role in the STE formation, while the remaining branches make a negligible contribution. This is similar to the phonon contribution to the hole polaron formation analyzed in the previous work [51]. However, there lies a major difference. For polaron formation, the long wavelength LO phonon dominates through long-range electron-phonon coupling [51]. Excitons, however, as a charge neutral quasiparticle, can interact with phonons not limited to the long wavelength modes. Thus, the contribution of different wave vectors of the LO phonon branch is almost evenly distributed, which is further illustrated in Figs. 3(d) and 3(e). There, we plot the averaged exciton-phonon coupling strength of the *K*-valley exciton, where short wavelength phonons with specific momenta show much stronger coupling compared to that at the Γ point.

Further, the real-space distortion is also computed and shown in Fig. 3(a), where the Be atoms are pushed away from the O atom, i.e., the localized hole, leading to a considerable bond length changing from 1.54 to 1.63 Å. Meanwhile, the hole seems to be more localized than the electron when the STE is formed (see SM Fig. S5 for comparison [34]), consistent with the existence of small hole polaron and absence of electron polaron in monolayer BeO. This implies the lattice distortion mainly traps the exciton through strong lattice-hole interaction, and the electron is trapped through strong Coulomb interaction with the trapped hole.

Finally, we note that monolayer BeO is an indirect gap semiconductor (SM Fig. S4 [34]), where the lowest exciton state is located at the *K* valley and has an energy 0.7 eV lower than the lowest bright exciton at the Γ point. In the same spirit of previous calculations, we may expect a huge Stokes shift of ∼1.1 eV. However, due to the indirect gap nature, STE in BeO has a much lower tendency to decay radiatively; thus, how it affects the photoluminescence will need further study.

Conclusions—We propose a theoretical and computational framework to treat the self-trapped excitons from first principles. Our method properly takes into account the electron-hole many-body interaction and their coupling to the full lattice degree of freedom using a combination of BSE and perturbation theory. Using a two-dimensional magnetic semiconductor $CrBr_3$ and a wide-gap indirect gap semiconductor BeO as prototype examples, we are able to quantitatively discuss the fine structure of the STE potential energy surfaces and compare them to the polaronic states. We also evaluate their Stokes shift energies that could readily be verified by the photoluminescence experiments. From the mode- and momentum-resolved coupling strength calculation, we pinpoint the phonon modes with significant contributions that could potentially be excited coherently and observed in transient absorption spectroscopy. Our work highlights the importance of lattice degree of freedom as well as the many-body effects, and further provides a general framework to effectively and efficiently make predictions of STE in real materials from first principles. Finally, the efficiency of our scheme can be significantly improved if the exciton-phonon coupling matrix can be interpolated using appropriate schemes, such as those employed for calculating the electron-phonon systems.

Note added—Recently, another group has independently developed a similar approach and has applied it to perovskite materials with important insights [52].

Acknowledgments—The authors thank National Natural Science Foundation of China (No. 12025407, No. 11934003, and No. 92250303), Ministry of Science and Technology (No. 2021YFA1400201), and Chinese Academy of Sciences (No. YSBR-047 and No. XDB33030100) for financial support.

[1] M. Selig, G. Berghäuser, A. Raja, P. Nagler, C. Schüller, T. F. Heinz, T. Korn, A. Chernikov, E. Malic, and A. Knorr, Nat. Commun. **7**, 13279 (2016).

[2] Z. Li, T. Wang, C. Jin, Z. Lu, Z. Lian, Y. Meng, M. Blei, S. Gao, T. Taniguchi, K. Watanabe, T. Ren, S. Tongay, L. Yang, D. Smirnov, T. Cao, and S.-F. Shi, Nat. Commun. **10**, 2469 (2019).

[3] D. Christiansen, M. Selig, G. Berghäuser, R. Schmidt, I. Niehues, R. Schneider, A. Arora, S. M. de Vasconcellos, R. Bratschitsch, E. Malic, and A. Knorr, Phys. Rev. Lett. **119**, 187402 (2017).

[4] H.-Y. Chen, D. Sangalli, and M. Bernardi, Phys. Rev. Res. **4**, 043203 (2022).

[5] J. Tan, D. Li, J. Zhu, N. Han, Y. Gong, and Y. Zhang, Nanoscale **14**, 16394 (2022).

[6] K. Edamatsu, M. Sumita, S. Hirota, and M. Hirai, Phys. Rev. B **47**, 6747 (1993).

[7] B. Yang and K. Han, J. Phys. Chem. Lett. **12**, 8256 (2021).

[8] Z. Xu, X. Jiang, H.-p. Cai, K. Chen, X. Yao, and Y. Feng, J. Phys. Chem. Lett. **12**, 10472 (2021).

[9] K. Song and R. T. Williams, *Self-Trapped Excitons*, Springer Series in Solid-State Sciences (Springer, Berlin, Heidelberg, 1996), 10.1007/978-3-642-85236-7.

[10] W. H. Sio, C. Verdi, S. Poncé, and F. Giustino, Phys. Rev. Lett. **122**, 246403 (2019).

[11] W. H. Sio, C. Verdi, S. Poncé, and F. Giustino, Phys. Rev. B **99**, 235139 (2019).

[12] J. M. Garcia-Lastra, J. D. Bass, and K. S. Thygesen, J. Chem. Phys. **135**, 121101 (2011).

[13] K. L. Seyler, D. Zhong, D. R. Klein, S. Gao, X. Zhang, B. Huang, E. Navarro-Moratalla, L. Yang, D. H. Cobden, M. A. McGuire, W. Yao, D. Xiao, P. Jarillo-Herrero, and X. Xu, Nat. Phys. **14**, 277 (2017).

[14] J. Dillon, H. Kamimura, and J. Remeika, J. Phys. Chem. Solids **27**, 1531 (1966).

[15] P. Grant and G. Street, Bull. Am. Phys. Soc. II **13**, 415 (1968).

[16] I. Pollini and G. Spinolo, Phys. Status Solidi (b) **41**, 691 (1970).

[17] V. M. Bermudez and D. S. McClure, J. Phys. Chem. Solids **40**, 129 (1979).

[18] L. Nosenzo, G. Samoggia, and I. Pollini, Phys. Rev. B **29**, 3607 (1984).

[19] W. Tao, C. Zhang, Q. Zhou, Y. Zhao, and H. Zhu, Nat. Commun. **12**, 1400 (2021).

[20] J. Zhang, X. Zhu, M. Wang, and B. Hu, Nat. Commun. **11**, 2618 (2020).

[21] L. Wang, Z. Shi, Z. Ma, D. Yang, F. Zhang, X. Ji, M. Wang, X. Chen, G. Na, S. Chen, D. Wu, Y. Zhang, X. Li, L. Zhang, and C. Shan, Nano Lett. **20**, 3568 (2020).

[22] J. Chen, J. Wang, X. Xu, J. Li, J. Song, S. Lan, S. Liu, B. Cai, B. Han, J. T. Precht, D. Ginger, and H. Zeng, Nat. Photonics **15**, 238 (2020).

[23] F. Meinardi, F. Bruni, and S. Brovelli, Nat. Rev. Mater. **2**, 17072 (2017).

[24] Y. Zhao and R. R. Lunt, Adv. Energy Mater. **3**, 1143 (2013).

[25] P. Erhart, A. Klein, D. Åberg, and B. Sadigh, Phys. Rev. B **90**, 035204 (2014).

[26] C. Spreafico and J. VandeVondele, Phys. Chem. Chem. Phys. **16**, 26144 (2014).

[27] X. Li, A. Wang, H. Chen, W. Tao, Z. Chen, C. Zhang, Y. Li, Y. Zhang, H. Shang, Y.-X. Weng, J. Zhao, and H. Zhu, Nano Lett. **22**, 8755 (2022).

[28] M. S. Hybertsen and S. G. Louie, Phys. Rev. B **34**, 5390 (1986).

[29] M. Rohlfing and S. G. Louie, Phys. Rev. B **62**, 4927 (2000).

[30] A. Ramasubramaniam, Phys. Rev. B **86**, 115409 (2012).

[31] J. P. Perdew, R. G. Parr, M. Levy, and J. L. Balduz, Phys. Rev. Lett. **49**, 1691 (1982).

[32] G. Antonius and S. G. Louie, Phys. Rev. B **105**, 085111 (2022).

[33] H.-Y. Chen, D. Sangalli, and M. Bernardi, Phys. Rev. Lett. **125**, 107401 (2020).

[34] See Supplemental Material at http://link.aps.org/supplemental/10.1103/PhysRevLett.133.046903 for a detailed discussion on our simulation workflow, computational details, benchmark of Li_2O_2, and results for $CrCl_3$ etc., which includes Refs. [35–47].

[35] J. P. Perdew, K. Burke, and M. Ernzerhof, Phys. Rev. Lett. **77**, 3865 (1996).

[36] P. Giannozzi *et al.*, J. Phys. Condens. Matter **29**, 465901 (2017).

[37] P. Giannozzi, S. Baroni, N. Bonini, M. Calandra, R. Car, C. Cavazzoni, D. Ceresoli, G. L. Chiarotti, M. Cococcioni, I. Dabo *et al.*, J. Phys. Condens. Matter **21**, 395502 (2009).

[38] D. R. Hamann, Phys. Rev. B **88**, 085117 (2013).

[39] G. Pizzi *et al.*, J. Phys. Condens. Matter **32**, 165902 (2020).

[40] J.-J. Zhou, J. Park, I.-T. Lu, I. Maliyov, X. Tong, and M. Bernardi, Comput. Phys. Commun. **264**, 107970 (2021).

[41] D. Sangalli, A. Ferretti, H. Miranda, C. Attaccalite, I. Marri, E. Cannuccia, P. Melo, M. Marsili, F. Paleari, A. Marrazzo, G. Prandini, P. Bonfá, M. O. Atambo, F. Affinito, M. Palummo, A. Molina-Sánchez, C. Hogan, M. Grüning, D. Varsano, and A. Marini, J. Phys. Condens. Matter **31**, 325902 (2019).

[42] A. Marini, C. Hogan, M. Grüning, and D. Varsano, Comput. Phys. Commun. **180**, 1392 (2009).

[43] S. Acharya, D. Pashov, A. N. Rudenko, M. Rösner, M. van Schilfgaarde, and M. I. Katsnelson, npj 2D Mater. Appl. **6**, 33 (2022).

[44] F. Bruneval and X. Gonze, Phys. Rev. B **78**, 085125 (2008).

[45] J. S. Hummelshøj, J. Blomqvist, S. Datta, T. Vegge, J. Rossmeisl, K. S. Thygesen, A. C. Luntz, K. W. Jacobsen, and J. K. Nørskov, J. Chem. Phys. **132**, 071101 (2010).

[46] L. Zhu and L. Yang, Phys. Rev. B **101**, 245401 (2020).

[47] X. Cai, T. Song, N. P. Wilson, G. Clark, M. He, X. Zhang, T. Taniguchi, K. Watanabe, W. Yao, D. Xiao, M. A. McGuire, D. H. Cobden, and X. Xu, Nano Lett. **19**, 3993 (2019).

[48] Y. Bai, Y. Wang, and S. Meng, AISTE code: http://everest.iphy.ac.cn/aiste/.

[49] Z. Zhang, J. Shang, C. Jiang, A. Rasmita, W. Gao, and T. Yu, Nano Lett. **19**, 3138 (2019).

[50] H. Zhang, M. Holbrook, F. Cheng, H. Nam, M. Liu, C.-R. Pan, D. West, S. Zhang, M.-Y. Chou, and C.-K. Shih, ACS Nano **15**, 2497 (2021).

[51] W. H. Sio and F. Giustino, Nat. Phys. **19**, 629 (2023).

[52] Z. Dai, C. Lian, J. Lafuente-Bartolome, and F. Giustino, Phys. Rev. Lett. **132**, 036902 (2024).